Metaphase kinetochore movements are regulated by kinesin-8 motors and microtubule dynamic instability

Anna H. Klemm[a,†,‡], Agneza Bosilj[b,†], Matko Glunčić[b], Nenad Pavin[b,*], and Iva M. Tolić[a,c,*]
[a]Max Planck Institute of Molecular Cell Biology and Genetics, 01307 Dresden, Germany; [b]Department of Physics, Faculty of Science, University of Zagreb, 10000 Zagreb, Croatia; [c]Division of Molecular Biology, Ruđer Bošković Institute, 10000 Zagreb, Croatia

ABSTRACT During metaphase, sister chromatids are connected to microtubules extending from the opposite spindle poles via kinetochores to protein complexes on the chromosome. Kinetochores congress to the equatorial plane of the spindle and oscillate around it, with kinesin-8 motors restricting these movements. Yet, the physical mechanism underlying kinetochore movements is unclear. We show that kinetochore movements in the fission yeast *Schizosaccharomyces pombe* are regulated by kinesin-8-promoted microtubule catastrophe, force-induced rescue, and microtubule dynamic instability. A candidate screen showed that among the selected motors only kinesin-8 motors Klp5/Klp6 are required for kinetochore centering. Kinesin-8 accumulates at the end of microtubules, where it promotes catastrophe. Laser ablation of the spindle resulted in kinetochore movement toward the intact spindle pole in wild-type and *klp5Δ* cells, suggesting that kinetochore movement is driven by pulling forces. Our theoretical model with Langevin description of microtubule dynamic instability shows that kinesin-8 motors are required for kinetochore centering, whereas sensitivity of rescue to force is necessary for the generation of oscillations. We found that irregular kinetochore movements occur for a broader range of parameters than regular oscillations. Thus, our work provides an explanation for how regulation of microtubule dynamic instability contributes to kinetochore congression and the accompanying movements around the spindle center.

INTRODUCTION

During mitosis, proper segregation of genetic material requires that sister chromatids of each chromosome attach to microtubules (MTs) extending from the opposite spindle poles via kinetochores, protein complexes on the chromosome (Cheeseman and Desai, 2008). When a pair of sister kinetochores establishes this configuration, termed *biorientation*, they oscillate around the equatorial plane of the spindle (Skibbens *et al.*, 1993). During oscillations kinetochores are predominantly under tension (Nicklas, 1988; Waters *et al.*, 1996; Dumont *et al.*, 2012). Kinetochore oscillations have been observed in various organisms, including yeast, amphibians, and mammals (Wise *et al.*, 1991; Skibbens *et al.*, 1993; Nabeshima *et al.*, 1998).

In the fission yeast *Schizosaccharomyces pombe*, the spindle in prometaphase consists of roughly 20 MTs extending from each spindle pole body (SPB, centrosome equivalent in yeast), and each sister kinetochore interacts with two to four MTs (Ding *et al.*, 1993). In this phase, sister kinetochores move around the spindle center until they get separated and pulled to the opposite SPBs in anaphase

(Funabiki *et al.*, 1993). Kinetochore movements in fission yeast consist of a series of stochastic back-and-forth movements (Nabeshima *et al.*, 1998), which are less regular than in vertebrate cells (Skibbens *et al.*, 1993).

Kinetochore oscillations are regulated by kinesin-8 motors in fission yeast (Garcia *et al.*, 2002; West *et al.*, 2002; Mary *et al.*, 2015; Gergely *et al.*, 2016) and in human cells (Mayr *et al.*, 2007; Gardner *et al.*, 2008; Stumpff *et al.*, 2008; Hafner *et al.*, 2014). Depletion of kinesin-8 leads to oscillations with a larger amplitude, suggesting that kinesin-8 improves chromosome congression to the metaphase plate. Fission yeast has two kinesin-8 motors, Klp5 and Klp6, which form a heterodimer (West *et al.*, 2001). Deleting either motor protein or both impairs MT dynamics in the same manner (West *et al.*, 2001, 2002; Garcia *et al.*, 2002; Unsworth *et al.*, 2008; Tischer *et al.*, 2009), yet there are also particular mitotic defects specific to individual deletions (Gergely *et al.*, 2016). In addition to kinesin-8, other motor proteins influence kinetochore oscillations. Inactivation of the kinesin-5 motor protein Kif11/Eg5 leads to irregular oscillations with a small amplitude (Vladimirou *et al.*, 2013). Chromokinesins (Levesque and Compton, 2001; Stumpff *et al.*, 2012; Wandke *et al.*, 2012), the XMAP215 family member TOGp (Cassimeris *et al.*, 2009), the centromere protein H (CENP-H) (Amaro *et al.*, 2010), and the MT depolymerizing kinesin mitotic centromere-associated kinesin (MCAK) (Jaqaman *et al.*, 2010) are also required for regular chromosome oscillations.

Kinetochore movements on the spindle require forces. Kinetochores are attached to plus ends of MTs and thus depend on the MT plus-end dynamics (Gachet *et al.*, 2008), which includes MT growth and shrinkage, as well as the switch from growth to shrinkage, termed *catastrophe*, and the opposite switch, termed *rescue*. Shrinking MTs can exert pulling forces on kinetochores (Grishchuk *et al.*, 2005), which stabilize kinetochore-microtubule attachments (Li and Nicklas, 1995; Akiyoshi *et al.*, 2010). When pulling forces are exerted on shrinking MTs, their shrinkage velocity decreases, oppositely from growing MTs, whose growth velocity increases (Akiyoshi *et al.*, 2010; Volkov *et al.*, 2013). Growing MTs exert pushing forces when growing against an obstacle, which results in a decrease of growth velocity (Dogterom and Yurke, 1997).

MT dynamics is regulated by MT-associated proteins. In particular, kinesin-8 motors have been shown to accumulate at the MT plus end in a MT length-dependent manner, where they facilitate MT catastrophe and shrinkage in vitro and in vivo (Gupta *et al.*, 2006; Varga *et al.*, 2006, 2009; Mayr *et al.*, 2007; Grissom *et al.*, 2009; Tischer *et al.*, 2009; Erent *et al.*, 2012; Leduc *et al.*, 2012). The influence of these motors on MT dynamics has been explored theoretically (Hough *et al.*, 2009; Varga *et al.*, 2009; Tischer *et al.*, 2010; Reese *et al.*, 2011; Johann *et al.*, 2012; Leduc *et al.*, 2012; Melbinger *et al.*, 2012). Length-dependent accumulation of kinesin-8 on MT ends and regulation of catastrophe is responsible for the centering of the nucleus by MT pushing against the cell edge in interphase cells (Tolic-Norrelykke, 2010; Gluncic *et al.*, 2015) and may also be important for kinetochore centering on the spindle.

The mechanism of kinetochore oscillations and centering has been explored in several theoretical studies. An early model of oscillations in higher eukaryotic cells is based on force-dependent kinetics of MT attachment to and detachment from the kinetochore (Joglekar and Hunt, 2002). Studies of oscillations in budding yeast introduced force-dependent MT dynamics as a key MT property needed to generate oscillations (Sprague *et al.*, 2003; Gardner *et al.*, 2005), which was also used in models for higher eukaryotic cells (Civelekoglu-Scholey, 2006, 2013; Liu *et al.*, 2008; Armond *et al.*, 2015; Banigan *et al.*, 2015). Contrary to the assumption that tension at the MT-kinetochore interface promotes detachment of the MT (Joglekar and Hunt, 2002), another study assumed that the absence of tension stimulates detachment of the MT from the kinetochore, describing the activity of Aurora B kinase in fission yeast (Gay *et al.*, 2012). This model was extended by including a MT length-dependent pulling force (Mary *et al.*, 2015). Moreover, a recent model included the effect of kinesin-8 motors on MT dynamics, kinetochore attachment, and sliding force in the spindle (Gergely *et al.*, 2016). More complex mechanisms have been proposed for higher eukaryotic cells (Civelekoglu-Scholey *et al.*, 2006, 2013; Liu *et al.*, 2008; Armond *et al.*, 2015; Banigan *et al.*, 2015). However, the physical mechanism underlying metaphase chromosome movements is still under debate.
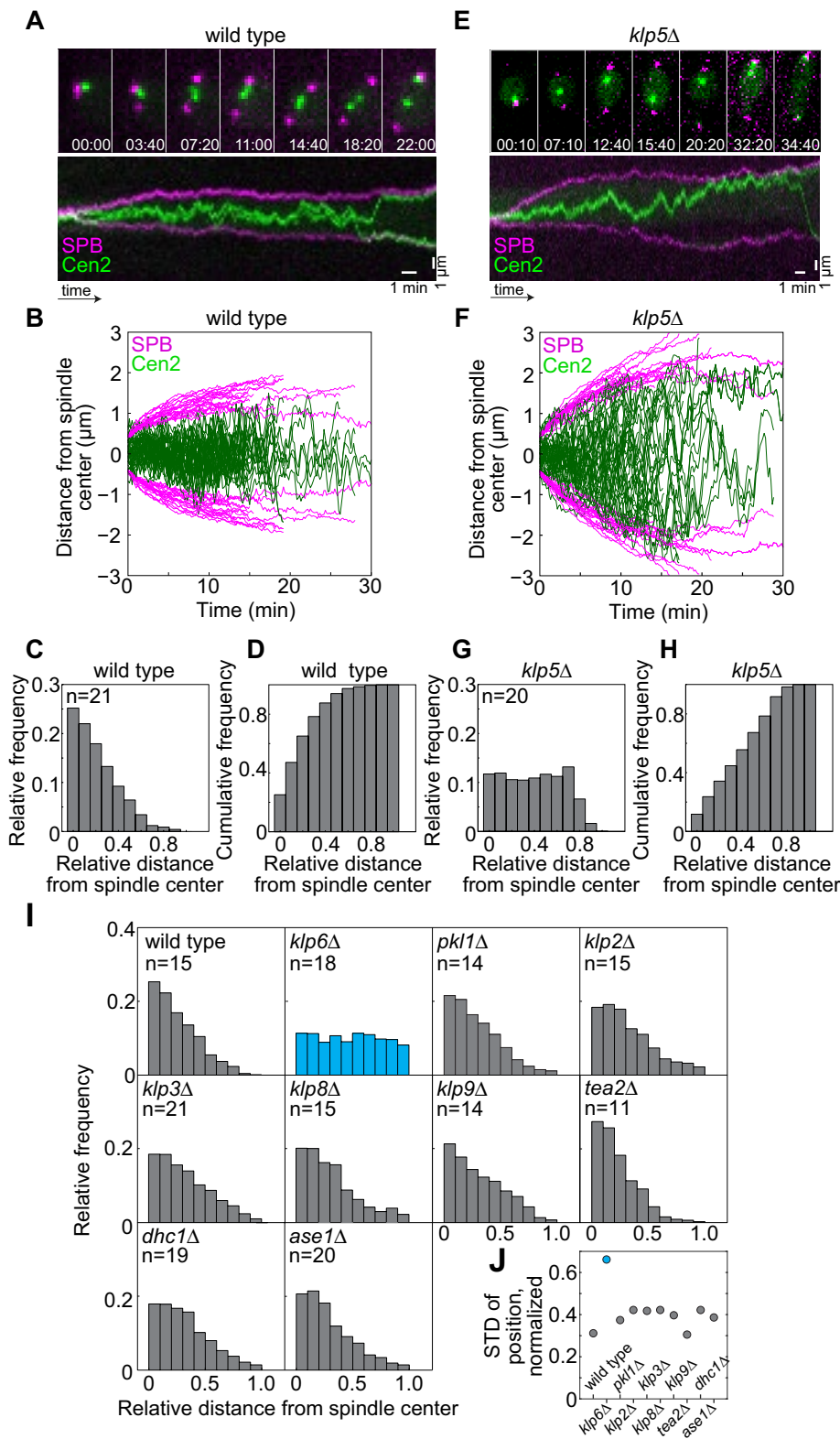
RESULTS

Kinesin-8 has a major role in restricting kinetochore movements around the spindle center

To study kinetochore movements in fission yeast, we used cells in which the SPBs were visualized by Sad1-dsRed and centromeres of chromosome 2 (Cen2) were marked by green fluorescent protein (GFP) (Figure 1A; see *Materials and Methods*). SPB labeling allowed us to follow the position of spindle ends and spindle length, whereas Cen2 labeling showed the position of a single pair of sister centromeres and therefore of the respective sister kinetochores assembled on these centromeres. We will refer to the Cen2 spots as kinetochores. By imaging mitosis from the beginning of prophase until the onset of anaphase, we observed that as the spindle elongates, which is visible as the separation of the two SPBs, the two sister kinetochores move along the spindle in a stochastic manner during metaphase and separate toward the opposite poles in anaphase (Figure 1A and Supplemental Movie S1). Quantification of kinetochore movements in metaphase (Figure 1B) showed that in 94% of all time frames, the midpoint between sister kinetochores was located in the central 50% of the spindle length (*n* = 2132 time frames in 21 cells; Figure 1, C and D). Thus, kinetochore movements are centered on the spindle in wild-type cells.

To explore the effect of kinesin-8 on kinetochore movements and positioning, we analyzed cells lacking Klp5 and found that kinetochores move in a stochastic manner as in wild type. However, contrary to wild type, kinetochores in *klp5Δ* cells are found along the whole spindle (Figure 1E and Supplemental Movie S2). Once moving, the kinetochores move to a larger extent than in wild type (Figure 1F). In only 67% of all time frames, the midpoint between sister kinetochores is found in the central 50% of the spindle length (*n* = 2080 time frames in 20 cells; Figure 1, G and H). To test whether the less efficient centering in *klp5Δ* cells is due to longer spindles in comparison with wild type, we analyzed in both strains spindles smaller than 1.47 µm (mean plus SD of spindle lengths in wild type). The SD of kinetochore position around the spindle center was 0.50 and 0.35 for *klp5Δ* and wild-type cells, respectively, calculated when the spindle length was normalized to the interval [–1,1]. These SDs are similar to those measured on spindles of all lengths, 0.53 and 0.34 for *klp5Δ* and wild-type cells, respectively, suggesting that the difference in centering efficiency is not due to differences in spindle length. Thus, Klp5 restricts kinetochore movements around the spindle center. This finding is consistent with previous studies in fission yeast (Mary *et al.*, 2015; Gergely *et al.*, 2016).

Next, we explored the role of other MT motor proteins in kinetochore movements and positioning during metaphase. We used a candidate approach in which we deleted individually all genes in the *S. pombe* genome that had been identified to have homology to the kinesin motor domain (Schoch *et al.*, 2003) and dynein heavy chain *dhc1* (Courtheoux *et al.*, 2007). We also deleted the nonmotor

cross-linker *ase1* (Loiodice *et al.*, 2005; Yamashita *et al.*, 2005). Note that the deletion of *cut7*, a kinesin-5 family member, was not studied because this deletion is lethal and inactivation of Cut7p in a temperature-sensitive mutant leads to spindle collapse (Hagan and Yanagida, 1992; Syrovatkina *et al.*, 2013). In each mutant, as well as in the respective wild-type strain, Cen2 was labeled with tdTomato and tubulin with GFP (Supplemental Table S1). We found that in all the mutants except the kinesin-8 *klp6Δ* the distribution of kinetochore position (Figure 1, I and J) and the general appearance of kinetochore movements (Supplemental Figure S1) were as in wild type. In the *klp6Δ* mutant, the distribution of kinetochore position was almost uniform along the spindle (Figure 1I), as in the *klp5Δ* mutant described above (Figure 1G). This result suggests that deletions of these two motor proteins have a similar effect on kinetochore movements and positioning, in agreement with a previous study (Mary *et al.*, 2015), and thus we focused on Klp5 in other experiments. We conclude that in *S. pombe* kinesin-8 motors Klp5/Klp6 have a major role in limiting kinetochore movements to the central region of the spindle, whereas other kinesins, dynein and Ase1, do not influence these movements significantly.

Polar microtubules undergo catastrophe less often and shrink faster in *klp5Δ* cells than in wild type

We next aimed to determine the effect of Klp5 on MT dynamics during mitosis. We focused on polar MTs, i.e., intranuclear MTs that grow from the SPB at an oblique angle with respect to the spindle during prometaphase (Zimmerman *et al.*, 2004; Vogel *et al.*, 2007; Kalinina *et al.*, 2013). The advantage of polar MTs for the measurement of MT dynamics is that their plus end is located away from the spindle and thus can be followed without interference of the signal from interpolar and kinetochore MTs. Moreover, polar MTs are free of forces generated at kinetochores or in overlap zones, which

used; *n* is the number of cells. (D) Cumulative histogram of the data in C. (E–H) Kinetochore movements and positioning in *klp5Δ* cells (strain AK06, *n* = 20), legend as in A–D, respectively. See Supplemental Movie S2. (I) Histograms of kinetochore position along the spindle in the indicated genetic backgrounds (strains AK30-AK39), legend as in C. (J) SD of kinetochore position around the spindle center for the strains from panel I, calculated when the spindle length was normalized to the interval [–1,1].
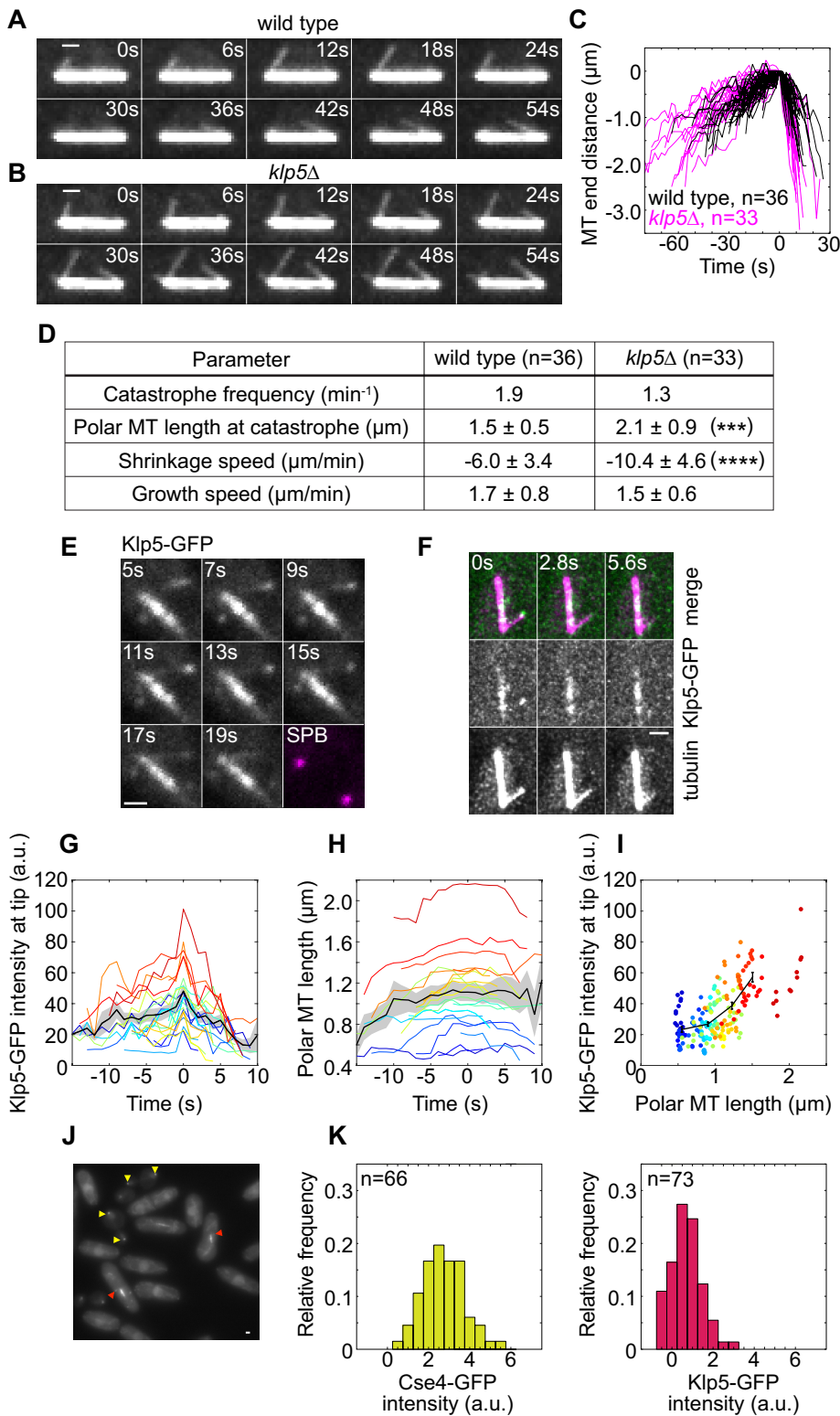
FIGURE 1: Kinesin-8 has a major role in kinetochore centering in *S. pombe*. (A–D) Kinetochore movements and positioning in wild-type cells. (A) Selected images (top) and kymograph (bottom) from a movie of mitosis in a wild-type cell (strain PD01) expressing Cen2-GFP (green) and Sad1-dsRed (magenta). Time is given in min:s; scale bar, 1 μm. See Supplemental Movie S1. (B) Distance from the spindle center of Cen2 (green) and SPBs (magenta) as a function of time for 21 wild-type cells (strain PD01). (C) Histogram of kinetochore position along the spindle (0 denotes spindle center, 1 denotes the SPB). The positions of the center between sister kinetochores in all time frames for spindles longer than 0.8 μm until the onset of anaphase were

FIGURE 2: Klp5 promotes catastrophe of polar MTs and accumulates on the plus ends in a MT length-dependent manner. (A, B) Time-lapse images of the mitotic spindle with polar MTs in a wild-type (A) and klp5Δ (B) cell. Cells express mCherry-atb2 (strains AK19 and AK20). Scale bars, 1 μm. (C) Length of polar MTs (distance between the plus end and SPB) in wild-type (black) and klp5Δ (magenta) cells as a function of time. The data are aligned so that the distance and time at MT catastrophe are 0. (D) Summary of polar MT dynamics in wild-type and klp5Δ cells; $p = 4 \times 10^{-5}$ (****), $p = 7 \times 10^{-4}$ (***). (E) Time-lapse images (sum projections) of a mitotic spindle in a cell expressing Klp5-GFP (white) and Sad1-dsRed (magenta, strain AK40). The image of SPBs (magenta) was recorded shortly before recording the time series of Klp5-GFP. The images of

may affect MT dynamics, contrary to the MTs extending between the SPBs. Note that the structure that appears as a polar MT may be a bundle of a few MTs; thus our measurements correspond to the longest MT in the bundle.

We imaged polar MTs in wild-type and klp5Δ cells expressing mCherry-atb2 to visualize MTs (Figure 2, A and B) and analyzed their length in time (Figure 2C). We found that the catastrophe frequency is lower in klp5Δ cells than in wild type (Figure 2D). In klp5Δ cells the MTs grew to a longer length before undergoing catastrophe than in wild type (Figure 2D). Sixty-seven percent of wild-type polar MTs underwent catastrophe at a length that corresponds to the central third of the spindle (average spindle length 2.9 ± 0.9 μm, central third: 1.0–1.9 μm, $n = 36$ cells). In klp5Δ cells, only 45% of polar MTs underwent catastrophe at a length corresponding to the central third of klp5Δ spindles (average spindle length 4.1 ± 1.1 μm,

Klp5-GFP were bleach-corrected (see *Materials and Methods*). Scale bar, 1 μm. See Supplemental Movie S3. (F) Deconvolved time-lapse wide-field fluorescence images (maximum projections) of a mitotic spindle in a cell expressing Klp5-GFP (green) and Atb2-mCherry (magenta, strain AK15). Merged images (top), Klp5-GFP (middle) and Atb2-mCherry (bottom) are shown. Scale bar, 1μm, time interval 2.8 s. (G) Klp5-GFP intensity (bleach corrected) at the tip of a polar MT and (H) length of polar MTs as a function of time, for 21 polar MTs. Each MT is shown in a color corresponding to its average length, from blue for short MTs to red for long MTs. Time 0 is defined as the time of the maximal Klp5-GFP intensity. The black curve shows the average values and the gray area denotes SEM. (I) Klp5-GFP intensity (bleach corrected) at the tip of a polar MT as a function of polar MT length, for the same polar MTs shown in the same colors as in panels G and H. Data for individual MTs are plotted from start of the measurements until the peak of Klp5-GFP intensity. The black curve shows the average values of the binned data; error bars, SEM. Note that the outlier (the longest MT) was not included in the average. (J) Wide-field fluorescence image (sum projection) of *S. pombe* cells expressing Klp5-GFP (strain AK18, red arrows show Klp5-GFP on polar MTs) together with *S. cerevisiae* cells expressing Cse4-GFP (strain KBY7006, yellow arrows show Cse4-GFP at spindle poles in anaphase). Scale bar, 1 μm. (K) Histograms of Cse4-GFP signal intensities at anaphase poles (yellow) and Klp5-GFP at polar MT tips (red). Mean ± SEM for Cse4-GFP was 3.4 ± 1.0 a.u. ($n = 66$), and 1.4 ± 0.8 a.u. ($n = 73$) for Klp5-GFP.

central third: 1.3–2.7 μm, *n* = 33 cells). Moreover, the shrinkage speed of polar MTs in *klp5Δ* cells was higher than in wild type, whereas the growth speeds were similar (Figure 2D). In summary, these data indicate that Klp5 promotes catastrophe and slows shortening of polar MTs.

Klp5 accumulates on the plus end of polar microtubules in a microtubule length-dependent manner, reaching a number of roughly 30 molecules

To understand how kinesin-8 motors are distributed along MTs in mitosis, we used cells expressing Klp5-GFP. We found Klp5 in a spotted pattern along the spindle (Figure 2, E and F). Because it was not possible in our assay to relate these Klp5 spots with the length of the MT to which Klp5 is bound, we again turned to polar MTs. We observed Klp5-GFP accumulating on the growing plus end of polar MTs (Figure 2E). Klp5-GFP signal intensity reached a maximum before the polar MT started to shrink (examples are shown in Figure 2, E and F, and quantification in Figure 2, G and H). Klp5-GFP signal intensity increased with increasing length of the polar MTs (Figure 2I), in agreement with previous measurements (Mary *et al.*, 2015). The increase in intensity was much faster for individual MTs than the increase averaged over several MTs (compare the slopes of colored data sets representing individual polar MTs and the slope of the black line representing the average in Figure 2I).

To estimate the average number of Klp5-GFP molecules on MT tips, we compared the signal intensity of Klp5-GFP spots with a signal intensity for which the corresponding number of molecules is known, following the approach from previous work (Ananthanarayanan *et al.*, 2013). We imaged exponentially growing fission yeast cells expressing Klp5-GFP and budding yeast cells expressing GFP-tagged histone H3-like centromere protein Cse4 in the same field of view (Figure 2J). In each budding yeast cell there are four to five Cse4 molecules per kinetochore (Coffman *et al.*, 2011; Lawrimore *et al.*, 2011). During late anaphase, kinetochores are found in two equal clusters, each close to one spindle pole. Each cluster contains 16 kinetochores and thus 64–80 Cse4 molecules. We found that the average signal intensity of Klp5-GFP on the tip of a polar MT was 2.43 lower than the signal intensity of Cse4-GFP at the spindle pole in anaphase (average Cse4-GFP intensity: 3.4 ± 1.0 a.u., *n* = 66; average Klp5-GFP intensity: 1.4 ± 0.8 a.u., *n* = 73; Figure 2K). Hence, we estimate that, on average, 26–33 Klp5-GFP molecules are located on the tip of a polar MT. Thus, our analysis of Klp5-GFP shows that Klp5 accumulates at the plus end of polar MTs in a MT length-dependent manner, typically reaching a number of 30 molecules.

Chromosome movements along the spindle are caused by pulling forces

To examine the forces acting on the kinetochores during metaphase in wild-type and *klp5Δ* cells, we performed laser ablation experiments of the spindle. We reasoned that if we destroy the MTs on one side of the sister kinetochores, their movement after ablation would provide information about the forces that act on the kinetochore. The metaphase spindle in wild-type cells is only 2–3 μm long, leaving not much space for ablation and for the subsequent movement of kinetochores. To increase the spindle size, we treated the cells with a low dose of hydroxyurea (Kim and Huberman, 2001). This treatment increased the spindle from 2.9 ± 0.9 μm to 3.6 ± 0.7 μm (*n* = 36 and 13 untreated and hydroxyurea-treated cells, respectively). This treatment did not affect the growth and shrinkage speed, catastrophe rate, and length at the time of catastrophe of polar MTs (Supplemental Figure S2), in agreement with previous results on interphase MTs (Tischer *et al.*, 2009).

We severed all spindle MTs on one side of the kinetochore pair, including interpolar and kinetochore MTs (Figure 3A). Spindle breakage and inward movement of the spindle poles were evidence for successful severing (Figure 3A), as previously described (Khodjakov *et al.*, 2004; Tolic-Norrelykke *et al.*, 2004; Raabe *et al.*, 2009; Maghelli and Tolic-Norrelykke, 2010, 2011). We found that in wildtype cells the kinetochores moved toward the SPB on the intact side of the spindle after ablation, irrespective of the kinetochore movement before ablation (*n* = 14 of 14 cells; Figure 3A, and Supplemental Figure S3A). This result is similar to previous observations that merotelic kinetochores move toward the intact side of the spindle after spindle ablation (Courtheoux *et al.*, 2009; Rumpf *et al.*, 2010; Cojoc *et al.*, 2016). We found that, after spindle ablation in *klp5Δ* cells, the kinetochores also moved toward the SPB on the intact side of the spindle (*n* = 10 of 10 cells; Figure 3B and Supplemental Figure S3A). These results suggest that kinetochores are moved by pulling forces in both wild-type and *klp5Δ* cells.

We then asked whether Klp5 motors affect the dynamics by which the kinetochores are pulled back toward the SPB after ablation. Poleward movement of the kinetochores started either immediately after ablation or after a short pausing time (Figure 3C). We did not detect a significant difference in the pausing time between wild-type and *klp5Δ* cells (13 ± 8 s and 16 ± 12 s, respectively; *p* = 0.49). Furthermore, poleward velocity of the kinetochores after ablation was similar in both cell types (–2.2 ± 0.5 μm/min for wild-type, –2.5 ± 0.7 μm/min for *klp5Δ*, *p* = 0.14; Figure 3D), suggesting a similar shrinkage speed of kinetochore MTs in the presence or absence of Klp5.

Finally, we tested whether pulling forces that move the kinetochores poleward after ablation are generated at the depolymerizing MT tip or along the MT. After ablation, we typically observed that as the kinetochore moved toward the SPB on the intact side of the spindle, the MT signal intensity between the kinetochore and that SPB was high, whereas the signal between the kinetochore and the ablation site was low (Figure 3E; additional examples are shown in Supplemental Figure S3B). We interpret the high MT signal as that of kinetochore MTs attached to the Cen2-labeled kinetochores together with other spindle MTs, whereas the low MT signal corresponds to the latter group only. Thus, the transition from high to low MT signal intensity visualizes kinetochore MT depolymerization in time, indicating that depolymerizing MT tips pull kinetochores toward the SPB.

Theoretical model for kinetochore congression and movements

To explore the physical basis of chromosome congression and movements around the metaphase plate, we develop a one-dimensional theoretical model, which is depicted in Figure 4A. The main idea of our approach is to use Langevin description of the fluctuations in the number of growing and shrinking MTs attached to kinetochores. We choose Langevin approach because it is suitable for systems with fluctuations in the number of particles (Van Kampen, 1992) and allows us to explore the ability of the system to generate movements around the center. In our model, which is formulated in Figure 4B and *Materials and Methods*, movements of kinetochores are calculated by the force-balance equations. The numbers of growing and shrinking MTs dynamically change, where tension increases MT rescue and decreases MT catastrophe (Akiyoshi *et al.*, 2010). Catastrophe is increased by kinesin-8 motors at the plus end of the MT (Tischer *et al.*, 2009), and the dynamics of motors along the MT length is described by the mean-field approximation, as for the motors on interphase MTs (Tischer *et al.*, 2010; Gluncic *et al.*, 2015).
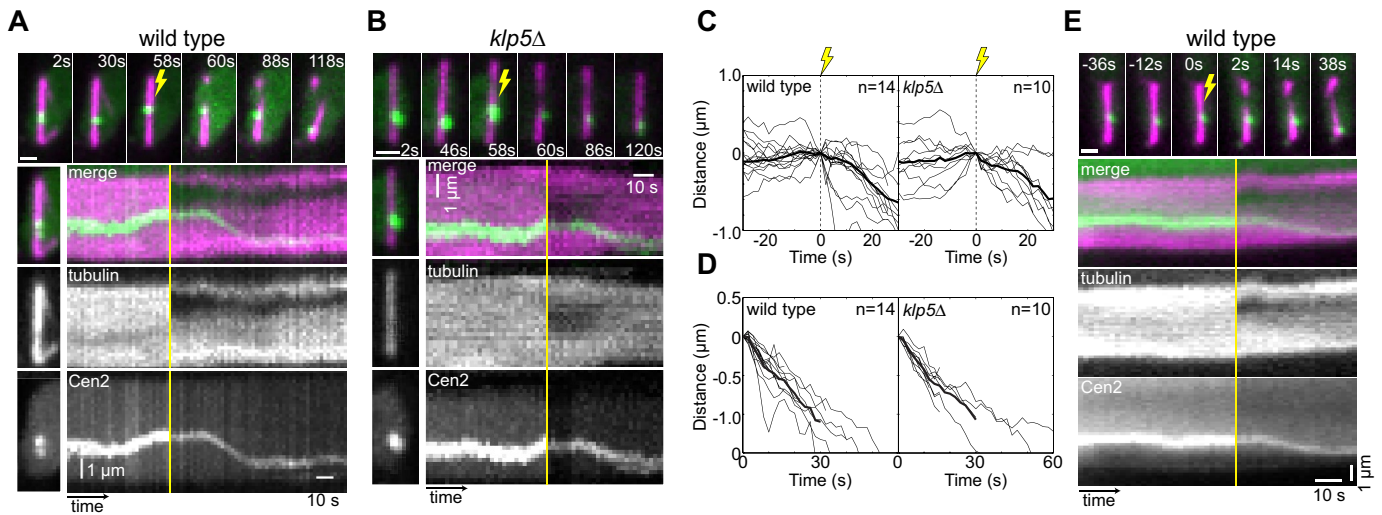
FIGURE 3: Spindle cutting shows that chromosome movements are driven by pulling forces. (A) Laser cutting of the spindle in a wild-type cell. Top, time-lapse images of a hydroxyurea-treated wild-type cell expressing Cen2-GFP (green) and mCherry-atb2 (magenta, strain AK20). Laser ablation is marked by the yellow lightning sign; time is given in seconds; scale bar, 1 μm. See Supplemental Movie S4. Below, kymographs of the area around the spindle (shown to the left of the kymograph) of the same cell are displayed (merged channels, mCherry-atb2, and Cen2-GFP from top to bottom). Yellow lines mark the time of laser ablation. Vertical and horizontal scale bars are 1 μm and 10 s, respectively. (B) Laser cutting of the spindle in a *klp5Δ* cell (strain AK19), legend as in A. See Supplemental Movie S5. (C) Kinetochore position along the spindle, with respect to its position at the time of ablation, before and after ablation in wild-type (*n* = 14, left) and *klp5Δ* (*n* = 10, right) cells. The data are aligned to the time of ablation (0 on abscissa) and position of the kinetochore one frame before ablation (0 on ordinate). Laser ablation is marked by the yellow lightning sign. The plot shows the closer sister kinetochore in cases where two kinetochores were detectable. Thick lines represent the mean. (D) Poleward movement of kinetochores toward the intact side of the spindle in wild-type (*n* = 14, left) and *klp5Δ* (*n* = 10, right) cells. The data are aligned to the time and kinetochore position just before the poleward movement starts (0 on abscissa and ordinate, respectively). For wild-type cells, a linear fit yielded a poleward speed of 2.2 ± 0.5 μm/min, and for *klp5Δ* cells 2.5 ± 0.7 μm/min (mean ± SD, *p* = 0.14). (E) Top, time-lapse images of a hydroxyurea-treated wild-type cell expressing Cen2-GFP (green) and mCherry-atb2 (magenta, strain AK20). Laser ablation is marked by the yellow lightning sign; time is given in seconds; scale bar, 1 μm, 0 is time of ablation. Kymographs of the same cell are displayed below (merged channels, mCherry-atb2, and Cen2-GFP from top to bottom); vertical and horizontal scale bars are 1 μm and 10 s, respectively.

Our model has 15 parameters, 10 of which are taken from the literature or measured here (Figure 4C). To estimate the unknown values of the parameters that describe MT rescue, k_{r0} and f_r, and to explore the behavior of the model, we use the model without kinesin-8 motors, $c = 0$. Numerical simulations show that a kinetochore pair moves along the spindle while the direction of the movement changes stochastically (Figure 5A). The values of the unknown parameters were obtained by comparison with experimentally measured distribution of kinetochore position (Figures 5B and 1F and *Materials and Methods*). Our model predicts that without kinesin-8 motors, kinetochores spend a similar amount of time under compression (~60%) and under tension (~40%) (Figure 5C).
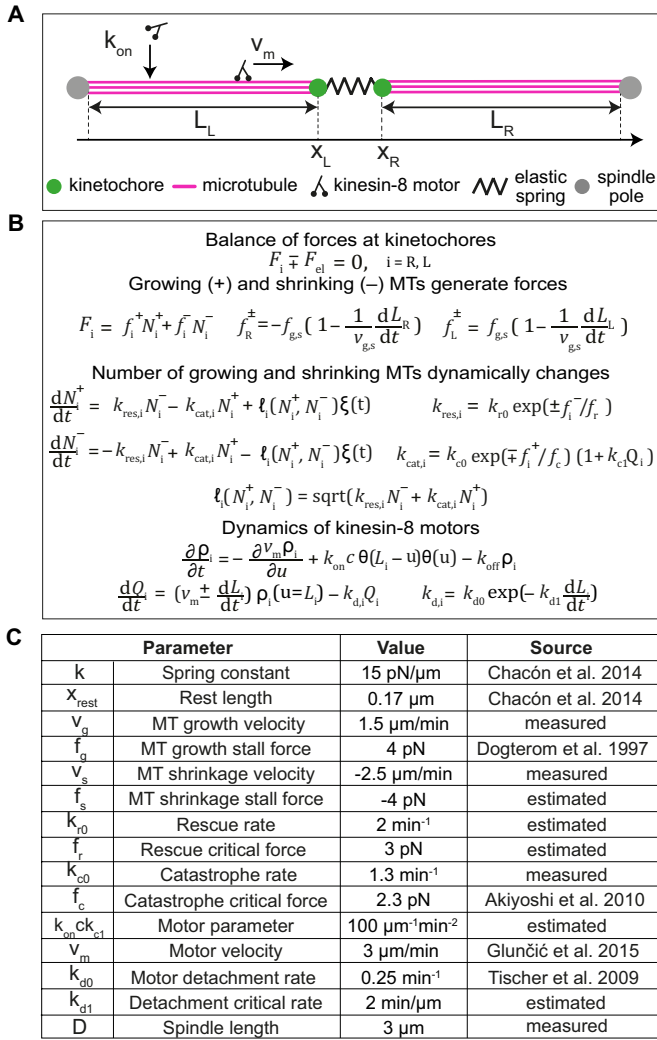
To determine the parameters that describe kinesin-8 motors, $k_{on}ck_{c1}$ and k_{d1}, we used a model with kinesin-8 motors. The parameter values were obtained by reproducing experimentally measured lengths of polar MTs and the number of kinesin-8 motors at their plus ends (Supplemental Figure S4, B–E, and *Materials and Methods*). Here, to describe polar MTs, we modified the model by setting the force at the MT plus end to zero. For the parameters in Figure 4C, our model provides a prediction for the movement and positioning of the kinetochores in cells with kinesin-8 motors. Numerical solutions of the model show that a kinetochore pair moves along the spindle with stochastic changes in the direction of movement (Figure 5D). However, in comparison with the model without motors (Figure 5A), the movement is more restricted to the central region of the spindle. This centering effect of motors is reflected in

the reduced SDs of kinetochore position as compared with the model without motors (compare Figure 5, B and E). The centering effect is due to accumulation of motors at the MT plus end in a MT length-dependent manner (Supplemental Figure S4D), which results in more catastrophes of longer MTs and thus less frequent excursions away from the spindle center. Kinetochores are predominantly under tension (98% of time, Figure 5F), in contrast to the model without kinesin-8 motors (see Figure 5C).

We compare the prediction from the model with experiments. The movements of kinetochores in experiments on wild-type cells are similar to those from the model (compare kymograph in Figure 1A with Figure 5D). The model also reproduces the histogram of kinetochore positions from experiments on wild-type cells (compare Figures 1C and 5E), providing a quantitative confirmation of the model prediction.

Next we explore how the model generates stochastic movements of kinetochores around the spindle center. To study the importance of the stochastic terms describing fluctuations in the number of growing and shrinking MTs, we investigate the movement of kinetochores in the case with and without stochastic terms (Figure 6). In the case without stochastic terms, our system attains stable oscillations around the spindle center or a fixed position at the center for different values of the motor concentration parameter (Figure 6A).

For small motor concentrations, kinetochores oscillate from one pole to the other (Figure 6A (I)). At intermediate concentrations, oscillations have a smaller amplitude and coexist together with a

A

B

Balance of forces at kinetochores

$$F_i \mp F_{el} = 0, \quad i = R, L$$

Growing (+) and shrinking (−) MTs generate forces

$$F_i = f_i^+ N_i^+ + f_i^- N_i^- \qquad f_R^\pm = -f_{g,s}\left(1 - \frac{1}{v_{g,s}}\frac{dL_R}{dt}\right) \qquad f_L^\pm = f_{g,s}\left(1 - \frac{1}{v_{g,s}}\frac{dL_L}{dt}\right)$$

Number of growing and shrinking MTs dynamically changes

$$\frac{dN_i^+}{dt} = k_{res,i}N_i^- - k_{cat,i}N_i^+ + \ell_i(N_i^+, N_i^-)\xi(t) \qquad k_{res,i} = k_{r0}\exp(\pm f_i^-/f_r)$$

$$\frac{dN_i^-}{dt} = -k_{res,i}N_i^- + k_{cat,i}N_i^+ - \ell_i(N_i^+, N_i^-)\xi(t) \qquad k_{cat,i} = k_{c0}\exp(\mp f_i^+/f_c)(1 + k_{c1}Q_i)$$

$$\ell_i(N_i^+, N_i^-) = \sqrt{k_{res,i}N_i^- + k_{cat,i}N_i^+}$$

Dynamics of kinesin-8 motors

$$\frac{\partial \rho_i}{\partial t} = -\frac{\partial v_m \rho_i}{\partial u} + k_{on}c\,\theta(L_i - u)\theta(u) - k_{off}\rho_i$$

$$\frac{dQ_i}{dt} = \left(v_m \pm \frac{dL_i}{dt}\right)\rho_i(u=L_i) - k_{d,i}Q_i \qquad k_{d,i} = k_{d0}\exp\left(-k_{d1}\frac{dL_i}{dt}\right)$$

C

	Parameter	Value	Source
k	Spring constant	15 pN/µm	Chacón et al. 2014
x_{rest}	Rest length	0.17 µm	Chacón et al. 2014
v_g	MT growth velocity	1.5 µm/min	measured
f_g	MT growth stall force	4 pN	Dogterom et al. 1997
v_s	MT shrinkage velocity	-2.5 µm/min	measured
f_s	MT shrinkage stall force	-4 pN	estimated
k_{r0}	Rescue rate	2 min^{-1}	estimated
f_r	Rescue critical force	3 pN	estimated
k_{c0}	Catastrophe rate	1.3 min^{-1}	measured
f_c	Catastrophe critical force	2.3 pN	Akiyoshi et al. 2010
$k_{on}ck_{c1}$	Motor parameter	100 µm^{-1}min^{-2}	estimated
v_m	Motor velocity	3 µm/min	Glunčić et al. 2015
k_{d0}	Motor detachment rate	0.25 min^{-1}	Tischer et al. 2009
k_{d1}	Detachment critical rate	2 min/µm	estimated
D	Spindle length	3 µm	measured

FIGURE 4: Theoretical model for metaphase kinetochore movements. (A) Scheme of the model. Kinetochores (green circles) connected by elastic spring (spring motive) are positioned at $x_{R,L}$. MTs (magenta lines) of lengths $L_{R,L}$, extend from the spindle poles (gray circles) to the kinetochores. Molecular kinesin-8 motors (black pictograms) attach at the MTs from nucleoplasm by constant rate k_{on} and walk toward MTs plus ends with velocity v_m. (B) Model equations. (C) Parameters of the model, see *Materials and Methods, Choice of parameter values.*

stable fixed point at the spindle center (Figure 6A (II)). For large concentrations, only a stable fixed point exists (Figure 6A (III)). Thus, for increasing concentrations an unstable fixed point becomes stable and our system undergoes a subcritical Hopf bifurcation (Figure 6B and *Materials and Methods*). The concentration range in which kinetochores oscillate without covering the whole spindle, similarly to kinetochore movement in wild-type cells, is narrow (Figure 6B, green). We conclude that our model with vanishing noise and biologically relevant parameters operates close to a subcritical Hopf bifurcation.

To explore the parameter space, we choose to vary the parameter related to motor concentration and the sensitivity of rescue to force. We find that the largest regions in the parameter space correspond to pole-to-pole oscillations (Figure 6C, red) and stable position in the spindle center (Figure 6C, blue). The range of motor concentrations for which the oscillations occur is broader for smaller values of the rescue critical force. Thus, the sensitivity of rescue to force promotes oscillations.

To test the influence of the stochastic terms on kinetochore movement, we explore the parameter space of the same parameters, without and with noise (Figure 6, C and D). Similarly to Figure 6B, in the case without noise the region in the parameter space corresponding to biologically relevant movements is narrow (Figure 6C, between red and blue regions). Interestingly, addition of the stochastic terms expands this region significantly (Figure 6D, orange to light blue). Thus, stochastic terms in our model ensure biologically relevant movements of kinetochores around the spindle center even for a large parameter variability.

DISCUSSION

Our model together with experiments suggests that kinesin-8 motors are required for kinetochore centering at the metaphase plate, whereas sensitivity of rescue to force is necessary for the generation of oscillations. Kinetochore centering is a consequence of accumulation of motors at the MT plus end in a MT length-dependent manner (Varga *et al.*, 2006), resulting in more catastrophes of longer MTs (Tischer *et al.*, 2009, 2010) and thus less frequent movements of kinetochore away from the spindle center.

In our model we use Langevin approach to describe stochastic nature of MT dynamic instability, which is the main difference in comparison to previous simulations of metaphase kinetochore movements in fission yeast (Gay *et al.*, 2012; Mary *et al.*, 2015; Gergely *et al.*, 2016) and in human cells (Civelekoglu-Scholey *et al.*, 2006, 2013; Liu *et al.*, 2008; Armond *et al.*, 2015; Banigan *et al.*, 2015). To describe stochasticity in MT dynamics, these previous models mainly used Monte Carlo simulations. By using Langevin approach, we found that kinetochore movement in the vicinity of metaphase plate occurs for a broad range of parameters only if MT dynamics is described in a stochastic manner. Similarly, the stochastic nature of the system ensures robustness of the dynamical behavior in rock-paper-scissors games (Reichenbach *et al.*, 2007). In our system the observed robustness of the kinetochore movements suggests that our model provides a plausible explanation for how a biological system with large variability generates typical kinetochore movements around the metaphase plate.
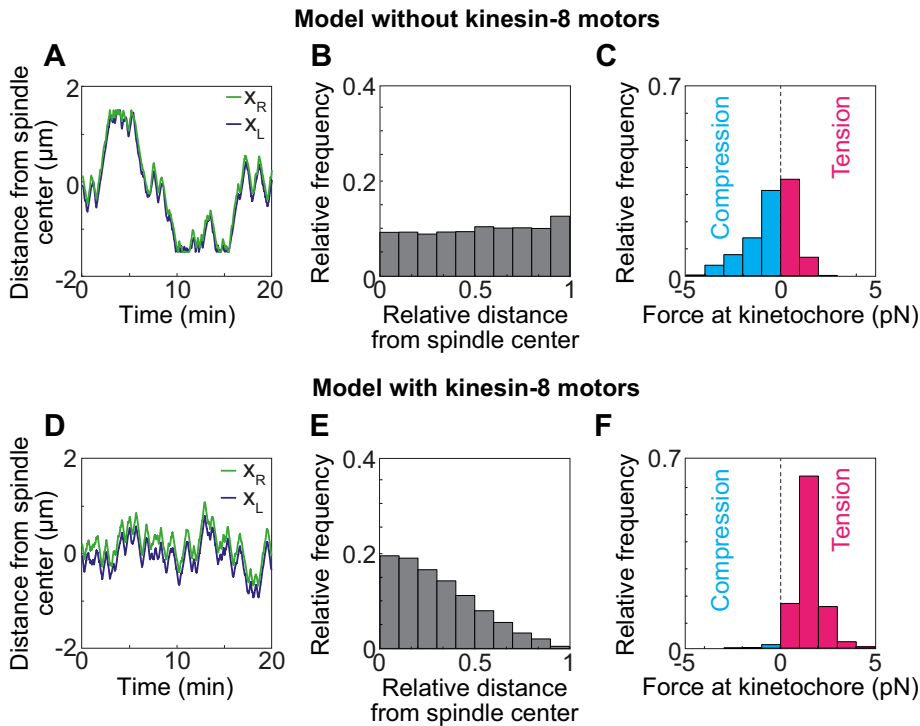
Our model can be extended to describe kinetochore congression to the metaphase plate and their oscillations in mammalian cells. In that case kinetochore fibers consist of roughly 20 MTs (McDonald *et al.*, 1992; Wendell *et al.*, 1993), for which we expect smaller influence of noise and therefore more regular oscillations. In addition to kinesin-8, which has been shown to enhance kinetochore centering, it will be necessary to include the bridging fiber in the model, because this fiber is laterally connected to the kinetochore fiber by passive cross-linkers (Vukusic *et al.*, 2017) and balances the tension between kinetochores (Kajtez *et al.*, 2016). A generalization of our model will reveal how these mechanisms contribute to kinetochore congression and the accompanying oscillations.

MATERIALS AND METHODS
Theoretical model

In our one-dimensional model we describe two oppositely oriented bundles of MTs connected to a pair of sister kinetochores (Figure 4A). The positions of the right and left kinetochore with respect to the cell center are denoted x_R and x_L, respectively. Subscripts R and L denote the right and left sides, respectively.

The movements of kinetochores at time *t* are calculated from balances of forces for each of them,

Model without kinesin-8 motors

A Distance from spindle center (μm) vs Time (min) — x_R (green), x_L (blue)

B Relative frequency vs Relative distance from spindle center

C Relative frequency vs Force at kinetochore (pN) — Compression / Tension

Model with kinesin-8 motors

D Distance from spindle center (μm) vs Time (min) — x_R (green), x_L (blue)

E Relative frequency vs Relative distance from spindle center

F Relative frequency vs Force at kinetochore (pN) — Compression / Tension

FIGURE 5: Results of the theoretical model for metaphase kinetochore movements. (A) Positions of the right (green) and left (blue) kinetochore shown as a function of time for the parameters given in Figure 4C for the model without the kinesin-8 motors, c = 0. (B) Distribution of the relative distance from spindle center of the central point between kinetochores. The SD of kinetochore position around the spindle center was 0.60, calculated when the spindle length was normalized to the interval [–1,1]. (C) Force at the kinetochore calculated for the model without kinesin-8 motors, c = 0. Negative force values correspond to the compression (light blue), while positive forces correspond to tension (red). (D) Position of the right (green) and left (blue) kinetochore shown as a function of time for the parameters given in Figure 4C. (E) Distribution of the relative distance from spindle center of the central point between kinetochores. The SD of kinetochore position around the spindle center was 0.37, calculated when the spindle length was normalized to the interval [–1,1]. (F) Force at the kinetochore calculated for the model with kinesin-8 motors. Color code as in C.

$$F_i \mp F_{el} = 0, \quad i = R, L. \tag{1}$$

Elastic force $F_{el} = k\Delta x$, is generated by the cohesin protein that connects sister kinetochores and is described as Hookean spring of stiffness k and extension $\Delta x = (x_R - x_L) - x_{rest}$, where x_{rest} denotes kinetochores rest length (Chacon et al., 2014). Total forces are generated by MT bundles in which contributions of growing and shrinking MTs are taken into account, $F_i = f_i^+ N_i^+ + f_i^- N_i^-$. Here N_i^+ and N_i^- denote number of growing and shrinking MTs, respectively. Total number of MTs attached to each kinetochores is same, $N_{tot} = N_i^+ + N_i^-$. Forces by which MTs act on the kinetochores are generated by MTs polymerization, f_i^+, and MTs depolymerization, f_i^-. These forces occur at MTs plus ends and are described by a linear force–velocity relationship,

$$f_R^{\pm} = -f_{g,s}\left(1 - \frac{1}{\upsilon_{g,s}}\frac{dL_R}{dt}\right) \tag{2a}$$

$$f_L^{\pm} = f_{g,s}\left(1 - \frac{1}{\upsilon_{g,s}}\frac{dL_L}{dt}\right) \tag{2b}$$

Here f_g denotes the force that stalls the MT growth and f_s denotes the force that stalls the MT shrinkage. Also, υ_g denotes MT growth velocity, while υ_g denotes MT shrinkage velocity in the absence of force. This linear force–velocity relationship is an approximation of the exponential force–velocity relationship measured in Akiyoshi et al. (2010) for both growth and shrinkage. Our linear force–velocity relationship approximates quantitatively the regime with forces smaller than the stall force, which is typical for our system: for example, when the left kinetochore is moving to the right, $dx_L/dt > 0$, the number of growing MTs is much larger than the number of shrinking MTs, $N_L^+ \gg N_L^-$, and the forces exerted by the growing MTs are much smaller than the stall force, $f_L^+ \ll f_g$ (Supplemental Figure S4A). An analogous argumentation holds for the case when the left kinetochore is moving to the left. MTs in our model are rigid and straight, and thus their lengths are calculated as $L_i = D/2 \mp x_i$, $i = R, L$, where D is spindle length. Growing MTs that are longer than spindle length, $L_i > D$, undergo catastrophes, whereas shrinking MTs of negative lengths $L_i < 0$ undergo rescue.

Numbers of growing and shrinking MTs in bundles change dynamically,

$$\frac{dN_i^+}{dt} = k_{res,i}\,N_i^- - k_{cat,i}N_i^+ \tag{3a}$$
$$+ \ell_i\left(N_i^+, N_i^-\right)\xi(t)$$

$$\frac{dN_i^-}{dt} = -k_{res,i}\,N_i^- + k_{cat,i}N_i^+ \tag{3b}$$
$$- \ell_i\left(N_i^+, N_i^-\right)\xi(t), \quad i = R, L$$

The rate of switching from shrinkage to growth, called rescue rate, increases when the force at the kinetochore increases (Akiyoshi et al., 2010),

$$k_{res,i} = k_{r0}\,\exp\left(\pm f_i^- / f_r\right), \quad i = R, L \tag{4}$$

Here k_{r0} denotes dependence of the rescue rate on the tension and f_r is the characteristic force of rescue. The rate of switching from growth to shrinkage, called catastrophe rate, is given as a function of the force and the number of kinesin-8 motors, $k_{cat,i}\left(f_i^+, Q_i\right) = f\left(f_i^+\right)g(Q_i)$. Using a Taylor expansion of the function $g(Q_i)$ to the first order, we approximate $g(Q_i) = 1 + k_{c1}Q_i$. Including the dependence of the catastrophe rate on force at the kinetochore (Akiyoshi et al., 2010), we calculate the catastrophe rate as

$$k_{cat,i} = k_{c0}\,\exp\left(\mp f_i^+ / f_c\right)\left(1 + k_{c1}Q_i\right), \quad i = R, L \tag{5}$$

Parameter k_{c0} denotes the catastrophe rate without force and f_c is characteristic force of the catastrophe. The second term describes increase of the catastrophe rate with the number of the kinesin-8 motors at the plus ends of the microtubules, Q_i and k_{c1} denotes to which extent 1 motor increases catastrophe rate. The Langevin terms in Eqs. 3a and 3b describe fluctuations in rescue and catastrophe events and are calculated as $\ell_i\left(N_i^+, N_i^-\right) = \sqrt{k_{res,i}N_i^- + k_{cat,i}N_i^+}$. Function $\xi(t)$ denotes Gaussian white noise, obeying $\xi(t) = 0$ and $\xi(t)\xi(t') = \delta(t - t')$, where δ is the Dirac delta function. Note that in the case without the stochastic terms, $\ell_i\left(N_i^+, N_i^-\right) = 0$, our model

A

B   C   STD   D
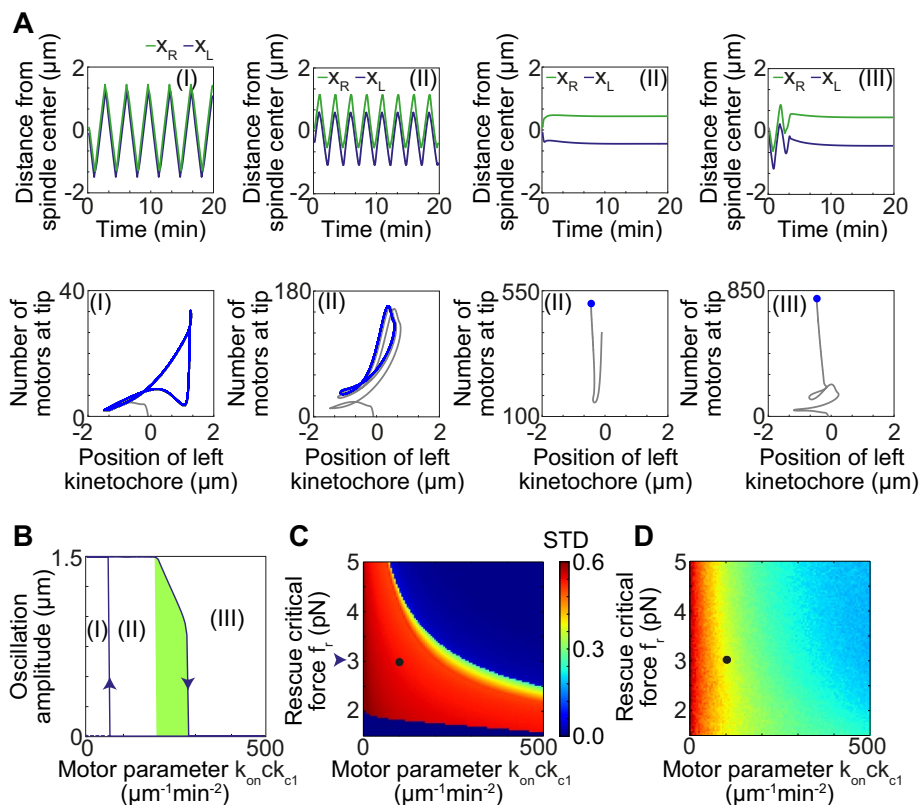
FIGURE 6: Influence of the Langevin terms on dynamic behavior of the model and parameter space. (A) Solutions of the model without the stochastic terms $\ell_i\left(N_i^+, N_i^-\right) = 0$ for different values of $k_{on}ck_{c1}$ and initial conditions. Top, positions of the right (green) and left (blue) kinetochore shown as s function of time. Bottom, phase plot of the number of kinesin-8 motors at the left MTs plus ends and the position of the left kinetochore (gray line), while stable limit cycle is marked by blue line and stable fixed point by blue circle. Parameters and initial conditions are (I) $k_{on}ck_{c1} = 50$ $\mu m^{-1}min^{-2}$, $Q_i = 0$; (II, left) $k_{on}ck_{c1} = 250$ $\mu m^{-1}min^{-2}$, $Q_i = 0$; (II, right) $k_{on}ck_{c1} = 250$ $\mu m^{-1}min^{-2}$, $Q_i = 400$; (III) $k_{on}ck_{c1} = 400$ $\mu m^{-1}min^{-2}$, $Q_i = 0$. (I)–(III) Other parameters are as in Figure 4C. Initial conditions are $x_{R, L} = \pm 0.1\mu m$, $N_R^+ = 2$, $N_{\bar{R}} = 1$, $N_L^+ = 1$, and $N_{\bar{L}} = 2$. (B) Bifurcation diagram for the model without the stochastic terms. The amplitude of right kinetochore movement is plotted for different values of $k_{on}ck_{c1}$. Hysteresis occurs in interval $k_{on}ck_{c1} \approx 60 - 275$ $\mu m^{-1}min^{-2}$. Stable pole-to-pole kinetochore oscillations (solid line) and the unstable fixed position (dashed line) occur in region I. Stable oscillations and the stable fixed position coexist in region II. Amplitude of oscillations decreases from pole-to-pole (white) to a smaller values (light green) in region II. Stable fixed position occurs in region III. Other parameters are as in Figure 4C. (C, D) Parameter space for the model without and with the stochastic terms, respectively. Colors denote values of the SD of the central point between kinetochores calculated when the spindle length was normalized to the interval [–1,1], as a function of $k_{on}ck_{c1}$ and f_r. For each point, equations are integrated for $t = 1000$ min. Grid size is 100×100. The same color bar applies to C and D. The black circle marks the position in the parameter space corresponding to Figure 4C. In C, arrowhead corresponds to the values of parameters investigated in B. In the dark blue area for $f_r < 2$ pN kinetochores oscillate in antiphase. Stochastic terms are described under *Materials and Methods*, section *Theoretical model*. Other parameters are as in Figure 4C.

becomes deterministic. We used reflective boundary condition in case if number of MTs decreases below zero or increases above total number of MTs at each kinetochore, N_{tot}.

To describe the distributions of kinesin-8 motors, we use a mean-field description by considering the motor density along the MT, $\rho_i(u, t)$. For a coordinate system with the origin at the kinetochore and the positive direction of the u coordinate in the direction of the plus end, in the low-density limit the motor density obeys

$$\frac{\partial \rho_i}{\partial t} = -\frac{\partial v_m \rho_i}{\partial u} + k_{on}c\theta\left(L_i - u\right)\theta(u) - k_{off}\rho_i, \quad i = R, L \qquad (6)$$

where the motors bind to and unbind from the MTs at the rates k_{on} and k_{off}, respectively (Tischer *et al.*, 2010). The concentration of the motors in the nucleoplasm is denoted c and the velocity of the motors is denoted v_m. The Heaviside step function θ ensures that the motors bind only along the MT. In the case when the motor velocity is larger than the MT growth velocity ($v_m > v_g$), the solution of the Eq. 6 reads

$$\rho_i(u)\big|_{u = L_i} = \frac{k_{on}c}{k_{off}} \left[1 - \exp\left(-\frac{k_{off}}{v_m}L_i\right)\right]$$

We use a limit of small motor unbinding rate in which this solution simplifies to

$$\rho_i(u)\big|_{u = L_i} = \frac{k_{on}c}{v_m} L_i$$

The number of motors at the plus end of the MTs is described as

$$\frac{dQ_i}{dt} = \left(v_m \pm \frac{dL_i}{dt}\right)\rho_i\big|_{u = L_i} - k_{d,i}Q_i, \quad i = R,L \qquad (7)$$

based on the experimentally observed accumulation of kinesin-8 motors at the plus end of growing MTs (Figure 2, E–G). As the intensity of the kinesin-8 motors decreases roughly three times during 10 s after reaching the maximum values, while MT length decreases 20% (Figure 2, G and H), we use an exponential dependence of the motor detachment rate on the shrinkage velocity, $k_{d,i} = k_{d0} \exp\left(-k_{d1}dL_i/dt\right)$, as a simplest function that changes faster than its input. Here k_{d0} denotes rate of motor detachment from the plus end of MT of a constant length, and k_{d1} denotes dependence of the rate of the detachment on the change of the MT length. This term ensures fast detachment of the motors from the MT plus end once the MT starts to shrink. We introduce a relative number of motors at the plus end as $q_i = Q_i/k_{on}c$, for which Eq. 7 becomes independent of parameters k_{on} and c. In this case, the second term in Eq. 5 reads $k_{c1}Q = k_{on}ck_{c1}q_i$. In our model, the parameters appear as one product, $k_{on}ck_{c1}$, which we use as one parameter. Differential equations 1–7 were integrated numerically in C++ programming language with time step $\Delta t = 0.1$ s for initial conditions given in Figure 4A.

Derivation of the Langevin terms. The Langevin terms are calculated for N MTs that are independent of each other and that stochastically switch between the growing and the shrinking state. In this case, we can represent the transition between the two states as random events that happen at certain rates. We denote by k_{res} the rate at which one MT switches from shrinking to growing and by k_{cat} the reverse transition. We assume that those transitions occur at constant rates, corresponding to an adiabatic approximation. This

means that there is a probability $k_{res}n\Delta t$ that one of the n MTs in the shrinking state switches from shrinking to growing in the time interval $(t, t + \Delta t)$. If there are N MTs in a bundle, then one of $(N - n)$ MTs in the growing state can switch from growing to shrinking with a probability of $k_{cat}(N - n)\Delta t$. By taking infinitesimally small time intervals in which only one event is possible (i.e., $\Delta t \rightarrow dt$, $(\Delta t)^2 \rightarrow 0$), we obtain the $N + 1$ differential equations describing the probability that there are n MTs in the shrinking state at time t, valid for $n = 0, 1, ..., N$,

$$\dot{p}_n = -\big(\Omega(n \rightarrow n-1) + \Omega(n \rightarrow n+1)\big)p_n + \Omega(n-1 \rightarrow n)p_{n-1} \quad (8)$$
$$+ \Omega(n+1 \rightarrow n)p_{n+1}$$

Here we introduce global rates of switching between global states with n MTs in a shrinking state

$$\Omega(n \rightarrow n+1) = (N - n)k_{cat} \quad (9a)$$

$$\Omega(n \rightarrow n-1) = nk_{res} \quad (9b)$$

Equation 8 is a master equation for the probability that the system is in the state with n shrinking MTs, p_n, where the first term is the loss of probability from state n to either $n - 1$ or $n + 1$, whereas the second and third terms represent the gain of probability from states with $n - 1$ or $n + 1$ MTs, respectively. We define the linear "step" operator E for any function $f(n)$ that depends on an integer variable n, as $E\big[f(n)\big] = f(n+1)$ and its powers as $E^l\big[f(n)\big] = f(n+l)$, for $l \in \mathbb{Z}$. Using operator E we rewrite master equation or define Langevin equation for the change of the number of MTs in the shrinking state as Eq. 10, where for $N \gg 1$, $F(n) = \sum_l l\Omega_{n \rightarrow n-l}$ and $G(n) = \sum_l l^2\Omega_{n \rightarrow n-l}$ are expected value and variance, respectively. The term $\sqrt{G(n)}$ corresponds to the Langevin terms in Eqs. 3a and 3b (Van Kampen, 1992)

$$\frac{dn(t)}{dt} = F(n) + \sqrt{G(n)}\xi(t) \quad (10)$$

Please note that the Eqs. 8 and 10 are obtained from fundamental principles and do not include additional parameters.

Choice of parameter values

The parameters of the model were taken from the literature, measured here, or determined as follows (Figure 4C). Values for k and x_{rest} are taken from Chacon et al. (2014) and are within the range of values used in Gay et al. (2012). Growth velocity in the absence of force, v_g, is measured here (Figure 2D). Note that this value is smaller than the one measured in Kalinina et al. (2013) and Blackwell et al. (2017), most likely because of a different number of MTs in the bundle and the different strains and temperatures used in those studies. Shrinkage velocity in the absence of force, v_s, is taken from ablation experiments, because the measured velocity of kinetochores in those experiments corresponds to the shrinkage velocity of kinetochore MTs in the absence of force from the opposite side (Figure 3D). Note that this value is smaller than the shrinkage velocity of polar MTs measured here (Figure 2D) and in Sagolla et al. (2003), Kalinina et al. (2013), and Blackwell et al. (2017). We choose MT shrinkage stall force to be the same as MT growth stall force. This choice does not influence the model behavior because the system is in the regime of forces smaller than the stall force. The catastrophe rate in the absence of force and kinesin-8 motors, k_{c0}, is taken from kinesin-8 deletion experiments (Figure 2D). Note that this value is smaller than the value from Blackwell et al. (2017). Other parameters that should be determined are k_{c0}, f_r, k_{d1} and the

product $k_{on}ck_{c1}$. By comparing our experimental and theoretical results for the distributions of kinetochore positions, in the case of kinesin-8 deletion (Figures 1 and 5), $c = 0$, and by comparing the lengths of the polar MTs in the case with kinesin-8 motors (see *Theory of polar MTs*), we obtain the values given in Figure 4C. Our values of the parameters k_{r0} and f_r are within the range of in vitro measurements, $k_{r0} = 1.43 \pm 0.47$ min^{-1} and $f_r = 6.4 \pm 4.2$ pN in Akiyoshi et al. (2010). Note that our value of k_{r0} is smaller than the value from Mary et al. (2015) and larger than the one from Blackwell et al. (2017).

Theory of polar MTs. The parameter that describes kinesin-8–dependent catastrophe, $k_{on}ck_{c1}$, was set to reproduce the experimentally measured lengths of the polar MTs (Supplemental Figure S4C). In our theory, polar MTs were modeled by setting parameters $F_{el} = 0$, $N_{tot} = 1$, and initial conditions $N_L^+ = 1$, $L_L = 0$, and $q_L = 0$. Note that we use $N_{tot} = 1$ because in our experiments we track most likely a single MT, namely the longest one in the bundle. We do not include forces generated by the interaction between the nuclear envelope and MTs to avoid extension of the model for the particular case of polar MTs. Equations were integrated without the stochastic terms. Using the experimental result that there are ~30 kinesin-8 motors at the MT tip before entering catastrophe, we were able to fix the value of parameters $k_{c1} = 2$ min^{-1} and the product $k_{on}c = 50$ µm^{-1} min^{-1}, giving the model parameter $k_{on}ck_{c1}$. The parameter that describes kinesin-8 motors detachment from the MTs, k_{d1}, was fixed to reproduce the experimental dependence of the number of kinesin-8 motors on MT length (Supplemental Figure S4, D and E). We find that for $k_{d1} = 2$ min/µm (Supplemental Figure S4D) the agreement with experiments (Figure 2I) was better than for $k_{d1} = 1$ min/µm and $k_{d1} = 5$ min/µm (Supplemental Figure S4E).

Strains and media

Fission yeast strains used in this study are listed in Supplemental Table S1. Cells were grown on yeast extract (YE) or Edinburgh minimal medium (EMM) with appropriate supplements at 25 ± 0.5°C in a Heraeus incubator (Thermo Scientific) (Forsburg and Rhind, 2006).

To construct strain AK06, *klp5* was deleted using the PCR gene-targeting method (Bahler et al., 1998). The *klp5* open reading frame (ORF) was hereby exchanged by homologous recombination with a NatMX-cassette (nourseothricin resistance). The primers were designed using the web tool www.bahlerlab.info/resources/ (Penkett et al., 2006).

Klp5-deletion-forward-primer: 5′GGTTATTGGAATTGTTGTTTG CGAGTGCCCTTCTTTTCATCTGTTTTGGATGATTGCTTG-CATGGAAATTTTGCTTTTCACGGATCCCCGGGGTTAATTAA3′

Klp5-deletion-reverse-primer: 5′ATCATCAAGCTTATCCGTTTTT TTTTTTTAAATATACCCAACAGGATATTTAGAGGATTCGTATTT-GAATATACGGACCTGAATTCGAGCTCGTTTAAAC3′

The primers contain 80 base pairs homologous to the flanking sequences directly before and after the ORF of Klp5 and 20 base pairs homologous to template plasmid pFa6a-NatMX. DNA fragments including the homology domains of Klp5 upstream and downstream region and the NatMX cassette were PCR amplified. The product of the PCR was purified using the QIAquick PCR Purification Kit for microcentrifuges (QIAGEN, Hilden, Germany) and then concentrated by isopropanol precipitation. The strain PD01 was transformed with the 15 µg Klp5-deletion-cassette, diluted in 15 µl 10 mM Tris-Cl, pH 8.5, by electroporation at 1.5 kV using an Eppendorf Electroporator 2510 (Eppendorf) (Forsburg and Rhind, 2006). Klp5-deleted strains were selected by growth

on YE + supplements + nourseothricin medium. Deletion was checked by PCR after DNA isolation (Forsburg and Rhind, 2006) using the following primers: 5′-CCATTCAAAACAAAGTGC-GTTA-3′ (forward); 5′- GGACCCATCCAGTGCCTCGAT-3′ (reverse inside NatMX-casette), as also DNA sequencing (sequencing primer: 5′-CCATTCAAAACAAAGTGCGTTA-3′).

Strains AK31-AK39 were generated by crossing of strains of the *S. pombe* Deletion Mutant Library (Bioneer) with strain PP682 (see Strains and Plasmid, Supplemental Table S1) following the Random Spore Analysis protocol (Forsburg and Rhind, 2006). For ectopic expression of GFP-atb2, cells were transformed with pREP81-GFP-atb2 using a chemical transformation method based on lithium acetate (Forsburg and Rhind, 2006). pREP81-GFP-atb2-transformed strains were selected with and kept on EMM lacking L-leucine, supplemented with 20 µM thiamine to suppress nmt81-promotor regulated GFP-atb2 expression.

Sample preparation

Cells were grown in YE liquid medium including the appropriate supplements overnight and the next day diluted 3–5 h before the measurements to achieve an exponentially growing culture. The cells were incubated on lectin-coated (L2380; Sigma-Aldrich) 35-mm glass-bottom culture dishes (MatTek Corporation) for 10 min for attachment and then washed with and kept in EMM supplemented with adenine, L-histidine, L-leucine, uracil, and L-lysine for live-cell imaging. All strains carrying pREP81-GFP-atb2 were grown in EMM lacking L-leucine supplemented with 1 µM thiamine during preparation and imaging. For hydroxyurea-treatment, hydroxyurea (H8627; Sigma-Aldrich) was added at a final concentration of 3 mM during preparation and imaging, according to the conditions used in a previous study (Tischer *et al.*, 2009).

Microscopy and laser ablation

Spinning disk confocal microscopy setup 1. Live-cell images were taken using an Andor Revolution Spinning Disk System (Andor Technology), consisting of a Yokogawa CSU-X1 spinning-disk scan head (Yokogawa Electric Corporation), connected to an Olympus IX81 inverted microscope (Olympus). The microscope was equipped with a Prior ProScanIII xy- scanning stage (Prior Scientific), a Prior NanoScanZ (Prior Scientific) and an Olympus UPlanSApo x100/1.35 NA oil objective (Olympus). The microscope was equipped with an iXon EM+ DU-897 BV back-illuminated electron-multiplying charge-coupled device (CCD) camera, cooled to –80°C (Andor Technology). The resulting *xy*-pixel size in the images was 81 nm. The system was controlled by Andor iQ2 software version 2.9 (Andor Technology). Excitation for imaging was done using a sapphire 488-nm solid-state laser (50 mW; Coherent) and a 561-nm solid-state laser (50 mW; Cobolt Jive). The laser power was controlled using the acousto-optic tunable filter in the Andor Revolution Laser Combiner (Andor Technology).

For recording chromosome oscillations in strains lacking kinesins, dhc1, or ase1, image stacks of 11 z-planes of 500-nm distance were taken at room temperature (22–24°C) with a time interval of 10 s, exposing sequentially for 100 ms with 15% of the 488-nm laser and 250 ms with 15% of the 560-nm laser within the time interval.

For recording Klp5-GFP on polar MTs, image stacks of 7 z-planes of 500-nm distance were taken at room temperature (22–24°C) with a time-interval of 1 s, exposing each plane for 100 ms with 50% of the 488-nm laser within the time interval. The Sad1-dsRed signal was recorded before and after recording the time-lapse series of Klp5-GFP, exposing for 200 ms with 27% of the 560-nm laser. A razor edge 488LP emission filter (Semrock) was used for the detection of the

Klp5-GFP signal and a razor edge 568LP emission filter (Semrock) for the Sad1-dsRed signal.

Spinning disk confocal microscopy setup 2 with a laser ablation module. Laser ablation experiments and imaging of basic chromosome oscillations of cen2-GFP/Sid4-dsRed-labeled strains were performed on a Yokogawa CSU10 spinning disk system (Yokogawa Electric Corporation) connected to an Olympus IX71 inverted microscope (Olympus) with an iXon EM+ DU-897 BV back-illuminated electron-multiplying CCD (Andor Technology), cooled to –80°C, electron multiplication gain 300. For excitation, a sapphire 488-nm solid-state laser (75 mW; Coherent) and a Jive 561-nm solid-state laser (75 mW; Cobolt) were used for GFP and tdTomato/dsRed, respectively. The laser intensity was controlled using the acousto-optic tunable filter inside the Andor Revolution Laser Combiner (Andor Technology). For sequential imaging, the emission wavelength was selected using respective emission filters BL 525/30 (Semrock) and ET 605/70 (Chroma) mounted in a fast, motorized filter wheel (Lambda-10B; Sutter Instrument Company). All images were recorded with an Olympus UPlanSApo × 100/1.4 NA oil objective (Olympus). The resulting xy-pixel size in the images was 174 nm; the z-distance between optical sections was 500 nm. The system was controlled by Andor iQ software version 2.9 (Andor Technology). The temperature was kept at 25°C using a Warner Heating Chamber (Warner Instruments).

For recording the oscillations of cen2-lacOp/lacI-GFP and Sid4-dsRed signals in wild-type and *klp5Δ* cells, image stacks of 15 z-planes of 500-nm distance were taken with a time interval of 10 s, exposing sequentially for 140 ms with 10% of the 488-nm laser and 210 ms with 10% of the 561-nm laser within the time interval.

For recording the oscillations of cen2-lacOp/lacI-GFP and pRep81-GFP-atb2 in limited candidate screen, image stacks of 11 z-planes of 500 nm distance were taken with a time interval of 10 s, exposing sequentially for 100 ms with 15% of the 488-nm laser and 200 ms with 18% of the 561-nm laser within the time interval.

For recording dynamics of atb2-mCherry-labeled polar MT of strains AK19 and AK20, image stacks of 7 z-planes of 500-nm distance were taken with a time interval of 2 s, exposing for 250 ms with 14.5% of the 561-nm laser. Cells were kept fixed to the glass slide using a 4% agarose in EMM + all amino acid agarose pad. AK19 and AK20 express the cen2-lacOp/lacI-GFP signal, which was checked in each cell before measurement to confirm metaphase.

For recording chromosome movements before and after ablation, image stacks of 5 z-planes of 500-nm distance were taken with a time interval of 2 s, exposing sequentially for 100 ms with 22% of the 488-nm laser and 100 ms with 20% of the 561-nm laser within the time-interval. Spindle severing was performed using a Micro-Point (Andor Technology) with 408-nm dye resonator cell.

Imaging of cells expressing Klp5-GFP together with S. cerevisiae cells expressing Cse4-GFP. Budding yeast cells (strain KBY7006) were grown on yeast peptone dextrose agar with kanamycin at 25 ± 0.5°C. Exponentially growing cells of strains AK18 and KBY7006 were mixed and imaged in a poly-L-lysine–coated glass bottom dish using a DeltaVision Microscope, equipped with an Olympus 100 × /1.40, UPLS Apo oil objective, using a GFP-filter cube, a 50% neutral density filter and an exposure time of 300 ms and 4x camera gain. Pixel size was 64 nm. Z-stacks of seven planes with 500-nm distance were recorded.

Widefield imaging of Klp5-GFP and Atb2-mCherry. Exponentially growing cells of strain AK15 were imaged in poly-L-lysine–coated

glass bottom dishes using a DeltaVision Microscope, equipped with a UPLS Apo × 100/1.40 NA oil objective. Klp5-GFP was imaged using a GFP-filter cube, Atb2-mCherry a mCherry filter cube. A 32% neutral density filter, an exposure time of 300 ms, and 4x camera gain was used for both channels.

Image processing and data analysis

Analysis of Klp5-GFP on polar MTs. For evaluation of the Klp5-GFP signal, sum projections of seven z-planes were bleach corrected using the Bleach Correction tool (Kota Miura and Jens Rietdorf) in Fiji (Schindelin *et al.*, 2012) using the exponential fitting method on the entire field of view. The first nine time frames were excluded from the data analysis due to unproportionally strong bleaching, presumably due to autofluorescent organelles. The tip of the polar MT in the bleach-corrected sum projection was tracked using the Low Light Tracking tool in Fiji (Krull *et al.*, 2014), giving the center and the intensity of the distal Klp5-GFP spot. For measuring the length of the polar MT, the position of the SPB (Sad1-dsRed) originating the polar MT was determined within the sum projection using the Low Light Tracking tool (Krull *et al.*, 2014), and the two-dimensional distance between SPB and polar MT tip was calculated. Data were further analyzed and plotted using scripts written in MAT-LAB (The Mathworks).

SPB and kinetochore tracking. Tracking of the centromeres/kinetochores of chromosome 2 (cen2-lacOp/lacI-GFP) and the spindle pole bodies (Sid4-GFP)/the ends of the spindle (pRep81-GFP-atb2) was performed on maximum projections of 15 z-planes (imaging conditions see above) using the Low Light Tracking tool in Fiji (Krull *et al.*, 2014). Sigma was set to 0.8 constant for centromere signals to 1.0 constant for SPB/spindle signals. Only cells that underwent complete metaphase and entered anaphase were analyzed. Data was further analyzed and plotted using scripts written in MATLAB (The Mathworks). The position of the kinetochore of chromosome 2 were determined relative to the center of the mitotic spindle, as a projection of the Cen2 position onto the spindle axis.

Histograms of kinetochore position. We calculated the midpoint between the sister kinetochores and the relative position of this midpoint along the spindle, defining the spindle center as 0 and the position of the closer SPB as +1. Evaluation was performed for all time frames from the time point when the spindle had reached a length of 0.8 μm until the onset of anaphase. The onset of anaphase was defined as the time point when the two sister kinetochores segregate completely, moving toward the SPBs without approaching each other again.

Analysis of polar MT dynamics. Z-stacks were maximum projected and the tip of the polar MT and the extreme ends of the spindle were manually tracked in Fiji using the Manual Tracking tool in Fiji (Fabrice Cordelières, Institut Curie, Orsay, France). Data were further analyzed and plotted using scripts written in MATLAB (The Mathworks). In a few cases (strain AK19: 5 of 52 events, strain AK20: 4 of 51 events), we measured a growth speed lower than 0.5 μm/min, which we considered as pausing, and we excluded those data from the analysis of growth and shrinkage dynamics. Catastrophe frequency was calculated considering the time spent from the start of growth until catastrophe.

Analysis of laser ablation experiments. The position of the kinetochores of chromosome 2 and the intact spindle end, that is, the end of the atb2-mCherry signal that is connected to the kineto-

chore, was tracked using the Low Light Tracking tool in Fiji (Krull *et al.*, 2014). Data were further analyzed and plotted using scripts written in MATLAB (The Mathworks). The distance between intact spindle pole body and the closer sister kinetochore was calculated. The speed of the poleward movement was calculated from the first time point after pausing (if present) until the kinetochore had reached a distance of 420 nm to the spindle end. The pausing time was manually determined. Only cells in which the spindle was clearly cut into two fragments were evaluated.

Quantification of the Klp5-GFP signal intensity by comparing it with the Cse4-GFP signal intensity in S. cerevisiae. Average pixel intensities of the sum projections were measured in a circular selection of 11 pixels diameter (708 nm), centered on the tip of polar MTs (*S. pombe*) or at the anaphase pole (*S. cerevisiae*).

Statistical analysis

Data are presented as mean ± SEM. For comparison of data sets, *t* test was used, with a significance level of 0.05. Data were analyzed in MATLAB (The Mathworks). Figures were assembled in Adobe Illustrator (Adobe Systems).

REFERENCES

Akiyoshi B, Sarangapani KK, Powers AF, Nelson CR, Reichow SL, Arellano-Santoyo H, Gonen T, Ranish JA, Asbury CL, Biggins S (2010). Tension directly stabilizes reconstituted kinetochore-microtubule attachments. Nature 468, 576–579.

Amaro AC, Samora CP, Holtackers R, Wang E, Kingston IJ, Alonso M, Lampson M, McAinsh AD, Meraldi P (2010). Molecular control of kinetochore-microtubule dynamics and chromosome oscillations. Nat Cell Biol 12, 319–329.

Ananthanarayanan V, Schattat M, Vogel SK, Krull A, Pavin N, Tolic-Norrelykke IM (2013). Dynein motion switches from diffusive to directed upon cortical anchoring. Cell 153, 1526–1536.

Armond JW, Harry EF, McAinsh AD, Burroughs NJ (2015). Inferring the forces controlling metaphase kinetochore oscillations by reverse engineering system dynamics. PLoS Comput Biol 11, e1004607.

Bahler J, Wu JQ, Longtine MS, Shah NG, McKenzie A 3rd, Steever AB, Wach A, Philippsen P, Pringle JR (1998). Heterologous modules for efficient and versatile PCR-based gene targeting in Schizosaccharomyces pombe. Yeast 14, 943–951.

Banigan EJ, Chiou KK, Ballister ER, Mayo AM, Lampson MA, Liu AJ (2015). Minimal model for collective kinetochore-microtubule dynamics. Proc Natl Acad Sci USA 112, 12699–12704.

Blackwell R, Sweezy-Schindler O, Edelmaier C, Gergely ZR, Flynn PJ, Montes S, Crapo A, Doostan A, McIntosh JR, Glaser MA, Betterton MD (2017). Contributions of microtubule dynamic instability and rotational diffusion to kinetochore capture. Biophys J 112, 552–563.

Cassimeris L, Becker B, Carney B (2009). TOGp regulates microtubule assembly and density during mitosis and contributes to chromosome directional instability. Cell Motil Cytoskeleton 66, 535–545.

Chacon JM, Mukherjee S, Schuster BM, Clarke DJ, Gardner MK (2014). Pericentromere tension is self-regulated by spindle structure in metaphase. J Cell Biol 205, 313–324.

Cheeseman IM, Desai A (2008). Molecular architecture of the kinetochore-microtubule interface. Nat Rev Mol Cell Biol 9, 33–46.

Civelekoglu-Scholey G, He B, Shen M, Wan X, Roscioli E, Bowden B, Cimini D (2013). Dynamic bonds and polar ejection force distribution explain kinetochore oscillations in PtK1 cells. J Cell Biol 201, 577–593.

Civelekoglu-Scholey G, Sharp DJ, Mogilner A, Scholey JM (2006). Model of chromosome motility in Drosophila embryos: adaptation of a general mechanism for rapid mitosis. Biophys J 90, 3966–3982.

Coffman VC, Wu P, Parthun MR, Wu JQ (2011). CENP-A exceeds microtubule attachment sites in centromere clusters of both budding and fission yeast. J Cell Biol 195, 563–572.

Cojoc G, Roscioli E, Zhang L, Garcia-Ulloa A, Shah JV, Berns MW, Pavin N, Cimini D, Tolic IM, Gregan J (2016). Laser microsurgery reveals conserved viscoelastic behavior of the kinetochore. J Cell Biol 212, 767–776.

Courtheoux T, Gay G, Gachet Y, Tournier S (2009). Ase1/Prc1-dependent spindle elongation corrects merotely during anaphase in fission yeast. J Cell Biol 187, 399–412.

Courtheoux T, Gay G, Reyes C, Goldstone S, Gachet Y, Tournier S (2007). Dynein participates in chromosome segregation in fission yeast. Biol Cell 99, 627–637.

Ding R, McDonald KL, McIntosh JR (1993). Three-dimensional reconstruction and analysis of mitotic spindles from the yeast, Schizosaccharomyces pombe. J Cell Biol 120, 141–151.

Dogterom M, Yurke B (1997). Measurement of the force-velocity relation for growing microtubules. Science 278, 856–860.

Dumont S, Salmon ED, Mitchison TJ (2012). Deformations within moving kinetochores reveal different sites of active and passive force generation. Science 337, 355–358.

Erent M, Drummond DR, Cross RA (2012). S. pombe kinesins-8 promote both nucleation and catastrophe of microtubules. PLoS One 7, e30738.

Forsburg SL, Rhind N (2006). Basic methods for fission yeast. Yeast 23, 173–183.

Funabiki H, Hagan I, Uzawa S, Yanagida M (1993). Cell cycle-dependent specific positioning and clustering of centromeres and telomeres in fission yeast. J Cell Biol 121, 961–976.

Gachet Y, Reyes C, Courtheoux T, Goldstone S, Gay G, Serrurier C, Tournier S (2008). Sister kinetochore recapture in fission yeast occurs by two distinct mechanisms, both requiring Dam1 and Klp2. Mol Biol Cell 19, 1646–1662.

Garcia MA, Koonrugsa N, Toda T (2002). Two kinesin-like Kin I family proteins in fission yeast regulate the establishment of metaphase and the onset of anaphase A. Curr Biol 12, 610–621.

Gardner MK, Odde DJ, Bloom K (2008). Kinesin-8 molecular motors: putting the brakes on chromosome oscillations. Trends Cell Biol 18, 307–310.

Gardner MK, Pearson CG, Sprague BL, Zarzar TR, Bloom K, Salmon ED, Odde DJ (2005). Tension-dependent regulation of microtubule dynamics at kinetochores can explain metaphase congression in yeast. Mol Biol Cell 16, 3764–3775.

Gay G, Courtheoux T, Reyes C, Tournier S, Gachet Y (2012). A stochastic model of kinetochore-microtubule attachment accurately describes fission yeast chromosome segregation. J Cell Biol 196, 757–774.

Gergely ZR, Crapo A, Hough LE, McIntosh JR, Betterton MD (2016). Kinesin-8 effects on mitotic microtubule dynamics contribute to spindle function in fission yeast. Mol Biol Cell 27, 3490–3514.

Gluncic M, Maghelli N, Krull A, Krstic V, Ramunno-Johnson D, Pavin N, Tolic IM (2015). Kinesin-8 motors improve nuclear centering by promoting microtubule catastrophe. Phys Rev Lett 114, 078103.

Grishchuk EL, Molodtsov MI, Ataullakhanov FI, McIntosh JR (2005). Force production by disassembling microtubules. Nature 438, 384–388.

Grissom P, Fielder T, Grishchuk E, Nicastro D, West RR, Mcintosh RJ (2009). Kinesin-8 from fission yeast: a heterodimeric, plus end-directed motor that can couple microtubule depolymerization to cargo movement. Mol Biol Cell 20, 963–972.

Gupta ML Jr, Carvalho P, Roof DM, Pellman D (2006). Plus end-specific depolymerase activity of Kip3, a kinesin-8 protein, explains its role in positioning the yeast mitotic spindle. Nat Cell Biol 8, 913–923.

Hafner J, Mayr MI, Mockel MM, Mayer TU (2014). Pre-anaphase chromosome oscillations are regulated by the antagonistic activities of Cdk1 and PP1 on Kif18A. Nat Commun 5, 4397.

Hagan I, Yanagida M (1992). Kinesin-related cut7 protein associates with mitotic and meiotic spindles in fission yeast. Nature 356, 74–76.

Hough LE, Schwabe A, Glaser MA, McIntosh JR, Betterton MD (2009). Microtubule depolymerization by the Kinesin-8 motor Kip3p: a mathematical model. Biophys J 96, 3050–3064.

Jaqaman K, King EM, Amaro AC, Winter JR, Dorn JF, Elliott HL, McHedlishvili N, McClelland SE, Porter IM, Posch M, et al. (2010). Kinetochore alignment within the metaphase plate is regulated by centromere stiffness and microtubule depolymerases. J Cell Biol 188, 665–679.

Joglekar AP, Hunt AJ (2002). A simple, mechanistic model for directional instability during mitotic chromosome movements. Biophys J 83, 42–58.

Johann D, Erlenkämper C, Kruse K (2012). Length regulation of active biopolymers by molecular motors. Phys Rev Lett 108, 258103.

Kajtez J, Solomatina A, Novak M, Polak B, Vukusic K, Rudiger J, Cojoc G, Milas A, Sumanovac Sestak I, Risteski P, et al. (2016). Overlap microtubules link sister k-fibres and balance the forces on bi-oriented kinetochores. Nat Commun 7, 10298.

Kalinina I, Nandi A, Delivani P, Chacon MR, Klemm AH, Ramunno-Johnson D, Krull A, Lindner B, Pavin N, Tolic-Norrelykke IM (2013). Pivoting of microtubules around the spindle pole accelerates kinetochore capture. Nat Cell Biol 15, 82–87.

Khodjakov A, La Terra S, Chang F (2004). Laser microsurgery in fission yeast; role of the mitotic spindle midzone in anaphase B. Curr Biol 14, 1330–1340.

Kim SM, Huberman JA (2001). Regulation of replication timing in fission yeast. EMBO J 20, 6115–6126.

Krull A, Steinborn A, Ananthanarayanan V, Ramunno-Johnson D, Petersohn U, Tolic-Norrelykke IM (2014). A divide and conquer strategy for the maximum likelihood localization of low intensity objects. Opt Express 22, 210–228.

Lawrimore J, Bloom KS, Salmon ED (2011). Point centromeres contain more than a single centromere-specific Cse4 (CENP-A) nucleosome. J Cell Biol 195, 573–582.

Leduc C, Padberg-Gehle K, Varga V, Helbing D, Diez S, Howard J (2012). Molecular crowding creates traffic jams of kinesin motors on microtubules. Proc Natl Acad Sci USA 109, 6100–6105.

Levesque AA, Compton DA (2001). The chromokinesin Kid is necessary for chromosome arm orientation and oscillation, but not congression, on mitotic spindles. J Cell Biol 154, 1135–1146.

Li X, Nicklas RB (1995). Mitotic forces control a cell-cycle checkpoint. Nature 373, 630–632.

Liu J, Desai A, Onuchic JN, Hwa T (2008). An integrated mechanobiochemical feedback mechanism describes chromosome motility from prometaphase to anaphase in mitosis. Proc Natl Acad Sci USA 105, 13752–13757.

Loiodice I, Staub J, Setty TG, Nguyen NP, Paoletti A, Tran PT (2005). Ase1p organizes antiparallel microtubule arrays during interphase and mitosis in fission yeast. Mol Biol Cell 16, 1756–1768.

Maghelli N, Tolic-Norrelykke IM (2010). Optical trapping and laser ablation of microtubules in fission yeast. Methods Cell Biol 97, 173–183.

Maghelli N, Tolic-Norrelykke IM (2011). Laser ablation of the microtubule cytoskeleton: setting up and working with an ablation system. Methods Mol Biol 777, 261–271.

Mary H, Fouchard J, Gay G, Reyes C, Gauthier T, Gruget C, Pecreaux J, Tournier S, Gachet Y (2015). Fission yeast kinesin-8 controls chromosome congression independently of oscillations. J Cell Sci 128, 3720–3730.

Mayr MI, Hummer S, Bormann J, Gruner T, Adio S, Woehlke G, Mayer TU (2007). The human kinesin Kif18A is a motile microtubule depolymerase essential for chromosome congression. Curr Biol 17, 488–498.

McDonald KL, O'Toole ET, Mastronarde DN, McIntosh JR (1992). Kinetochore microtubules in PTK cells. J Cell Biol 118, 369–383.

Melbinger A, Reese L, Frey E (2012). Microtubule length regulation by molecular motors. Phys Rev Lett 108, 258104.

Nabeshima K, Nakagawa T, Straight AF, Murray A, Chikashige Y, Yamashita YM, Hiraoka Y, Yanagida M (1998). Dynamics of centromeres during metaphase-anaphase transition in fission yeast: Dis1 is implicated in force balance in metaphase bipolar spindle. Mol Biol Cell 9, 3211–3225.

Nicklas RB (1988). The forces that move chromosomes in mitosis. Annu Rev Biophys Biophys Chem 17, 431–449.

Penkett CJ, Birtle ZE, Bahler J (2006). Simplified primer design for PCR-based gene targeting and microarray primer database: two web tools for fission yeast. Yeast 23, 921–928.

Raabe I, Vogel SK, Peychl J, Tolic-Norrelykke IM (2009). Intracellular nano-surgery and cell enucleation using a picosecond laser. J Microsc 234, 1–8.

Reese L, Melbinger A, Frey E (2011). Crowding of molecular motors determines microtubule depolymerization. Biophys J 101, 2190–2200.

Reichenbach T, Mobilia M, Frey E (2007). Mobility promotes and jeopardizes biodiversity in rock-paper-scissors games. Nature 448, 1046–1049.

Rumpf C, Cipak L, Schleiffer A, Pidoux A, Mechtler K, Tolic-Norrelykke IM, Gregan J (2010). Laser microsurgery provides evidence for merotelic kinetochore attachments in fission yeast cells lacking Pcs1 or Clr4. Cell Cycle 9, 3997–4004.

Sagolla MJ, Uzawa S, Cande WZ (2003). Individual microtubule dynamics contribute to the function of mitotic and cytoplasmic arrays in fission yeast. J Cell Sci 116, 4891–4903.

Schindelin J, Arganda-Carreras I, Frise E, Kaynig V, Longair M, Pietzsch T, Preibisch S, Rueden C, Saalfeld S, Schmid B, et al. (2012). Fiji: an open-source platform for biological-image analysis. Nat Methods 9, 676–682.

Schoch CL, Aist JR, Yoder OC, Gillian Turgeon B (2003). A complete inventory of fungal kinesins in representative filamentous ascomycetes. Fungal Genet Biol 39, 1–15.

Skibbens RV, Skeen VP, Salmon ED (1993). Directional instability of kinetochore motility during chromosome congression and segregation in mitotic newt lung cells: a push-pull mechanism. J Cell Biol 122, 859–875.

Sprague BL, Pearson CG, Maddox PS, Bloom KS, Salmon ED, Odde DJ (2003). Mechanisms of microtubule-based kinetochore positioning in the yeast metaphase spindle. Biophys J 84, 3529–3546.

Stumpff J, von Dassow G, Wagenbach M, Asbury C, Wordeman L (2008). The kinesin-8 motor Kif18A suppresses kinetochore movements to control mitotic chromosome alignment. Dev Cell 14, 252–262.

Stumpff J, Wagenbach M, Franck A, Asbury CL, Wordeman L (2012). Kif18A and chromokinesins confine centromere movements via microtubule growth suppression and spatial control of kinetochore tension. Dev Cell 22, 1017–1029.

Syrovatkina V, Fu C, Tran PT (2013). Antagonistic spindle motors and MAPs regulate metaphase spindle length and chromosome segregation. Curr Biol 23, 2423–2429.

Tischer C, Brunner D, Dogterom M (2009). Force- and kinesin-8-dependent effects in the spatial regulation of fission yeast microtubule dynamics. Mol Syst Biol 5, 250.

Tischer C, Ten Wolde PR, Dogterom M (2010). Providing positional information with active transport on dynamic microtubules. Biophys J 99, 726–735.

Tolic-Norrelykke IM (2010). Force and length regulation in the microtubule cytoskeleton: lessons from fission yeast. Curr Opin Cell Biol 22, 21–28.

Tolic-Norrelykke IM, Sacconi L, Thon G, Pavone FS (2004). Positioning and elongation of the fission yeast spindle by microtubule-based pushing. Curr Biol 14, 1181–1186.

Unsworth A, Masuda H, Dhut S, Toda T (2008). Fission yeast kinesin-8 Klp5 and Klp6 are interdependent for mitotic nuclear retention and required for proper microtubule dynamics. Mol Biol Cell 19, 5104–5115.

Van Kampen NG (1992). Stochastic Processes in Physics and Chemistry, Amsterdam: Elsevier Science.

Varga V, Helenius J, Tanaka K, Hyman AA, Tanaka TU, Howard J (2006). Yeast kinesin-8 depolymerizes microtubules in a length-dependent manner. Nat Cell Biol 8, 957–962.

Varga V, Leduc C, Bormuth V, Diez S, Howard J (2009). Kinesin-8 motors act cooperatively to mediate length-dependent microtubule depolymerization. Cell 138, 1174–1183.

Vladimirou E, McHedlishvili N, Gasic I, Armond JW, Samora CP, Meraldi P, Mcainsh AD (2013). Nonautonomous movement of chromosomes in mitosis. Dev Cell 27, 60–71.

Vogel SK, Raabe I, Dereli A, Maghelli N, Tolic-Norrelykke I (2007). Interphase microtubules determine the initial alignment of the mitotic spindle. Curr Biol 17, 438–444.

Volkov VA, Zaytsev AV, Gudimchuk N, Grissom PM, Gintsburg AL, Ataullakhanov FI, McIntosh JR, Grishchuk EL (2013). Long tethers provide high-force coupling of the Dam1 ring to shortening microtubules. Proc Natl Acad Sci USA 110, 7708–7713.

Vukusic K, Buda R, Bosilj A, Milas A, Pavin N, Tolic IM (2017). Microtubule sliding within the bridging fiber pushes kinetochore fibers apart to segregate chromosomes. Dev Cell 43, 11–23 e16.

Wandke C, Barisic M, Sigl R, Rauch V, Wolf F, Amaro AC, Tan CH, Pereira AJ, Kutay U, Maiato H, et al. (2012). Human chromokinesins promote chromosome congression and spindle microtubule dynamics during mitosis. J Cell Biol 198, 847–863.

Waters JC, Skibbens RV, Salmon ED (1996). Oscillating mitotic newt lung cell kinetochores are, on average, under tension and rarely push. J Cell Sci 109, 2823–2831.

Wendell KL, Wilson L, Jordan MA (1993). Mitotic block in HeLa cells by vinblastine: ultrastructural changes in kinetochore-microtubule attachment and in centrosomes. J Cell Sci 104, 261–274.

West RR, Malmstrom T, Mcintosh RJ (2002). Kinesins klp5(+) and klp6(+) are required for normal chromosome movement in mitosis. J Cell Sci 115, 931–940.

West RR, Malmstrom T, Troxell C, Mcintosh RJ (2001). Two related kinesins, klp5+ and klp6+, foster microtubule disassembly and are required for meiosis in fission yeast. Mol Biol Cell 12, 3919–3932.

Wise D, Cassimeris L, Rieder CL, Wadsworth P, Salmon ED (1991). Chromosome fiber dynamics and congression oscillations in metaphase PtK2 cells at 23 degrees C. Cell Motil Cytoskeleton 18, 131–142.

Yamashita A, Sato M, Fujita A, Yamamoto M, Toda T (2005). The roles of fission yeast ase1 in mitotic cell division, meiotic nuclear oscillation, and cytokinesis checkpoint signaling. Mol Biol Cell 16, 1378–1395.

Zimmerman S, Daga RR, Chang F (2004). Intra-nuclear microtubules and a mitotic spindle orientation checkpoint. Nat Cell Biol 6, 1245–1246.